Low-Cost, High-Resolution, Fault-Robust Position and Speed Estimation for PMSM Drives Operating in Safety-Critical Systems

Giulio De Donato, *Senior Member, IEEE*, Giacomo Scelba, *Senior Member, IEEE*, Mario Pulvirenti, *Member, IEEE*, Giuseppe Scarcella, *Senior Member, IEEE*, and Fabio Giulii Capponi, *Member, IEEE*

***Abstract*—In this paper, it is shown how to obtain a low-cost, high-resolution, and fault-robust position sensing system for permanent-magnet synchronous motor drives operating in safety-critical systems, by combining binary Hall-effect sensors with high-frequency signal injection. It is shown that the position error signal obtained via signal injection can be merged easily into the quantization-harmonic-decoupling vector-tracking observer that is used to process the Hall-effect sensor signals. The resulting algorithm provides accurate, high-resolution estimates of speed and position throughout the entire speed range; compared to the state-of-the-art drives using Hall-effect sensors alone, the low-speed performance is greatly improved in healthy conditions and also following position sensor faults. It is envisaged that such a sensing system can be successfully used in applications requiring IEC 61508 SIL 3 or ISO 26262 ASIL D compliance, due to its extremely high mean time to failure and to the very fast recovery of the drive following Hall-effect sensor faults at low speeds. Extensive simulation and experimental results are provided on a 3.7-kW interior permanent-magnet drive.**

***Index Terms*—Aerospace, automotive, brushless, fault tolerance, Hall effect, observer, permanent magnet, position sensor, redundancy, resolution, safety, self-sensing, sensorless, signal injection, synchronous motor.**

I. Introduction

ANGULAR position measurement of the rotor's magnetic field is necessary in permanent-magnet synchronous motor (PMSM) drives to achieve correct field orientation. It is well known that the required resolution of this measurement depends on whether the drive is of the brushless dc (BLDC) or of the brushless ac (BLAC) type. For the former, a 60 electrical degree resolution, i.e., 3 bits per pole pair (BPP), is sufficient to obtain a 120° rectangular wave current supply. On the other hand, the BLAC drive requires a much higher resolution to produce a sinusoidal current supply, in the range of 10–12 BPP; this is usually achieved by using optical encoders or electromagnetic resolvers. These high-resolution sensors are quite expensive and do not possess a very high robustness to faults, since their reported mean time to failure (MTTF) [1], [2] is usually in the range of $5\,10^5$–$2\,10^6$ h. This makes their use in drives operating in safety-critical systems, such as those found on aircrafts, vehicles, cranes, hoists, or wind turbines, particularly challenging. For these, international safety standards require less than one dangerous system failure every 10^7–10^9 h of operation [3]–[7]. For example, Table I reports four examples of hazardous events in a passenger vehicle, the associated Automotive Safety Integrity Level (ASIL) according to the ISO Standard 26262, the Safety Integrity Level (SIL) according to the IEC Standard 61508, and the acceptable dangerous failures per hour (DFH).

Not all failures are dangerous, and the correct value of DFH has to be calculated carefully, by following the guidelines indicated by the standards. Furthermore, the standards require the entire system to comply with the required safety integrity levels. Thus, as shown in [12], also the motor, the bearings, and the converter must have sufficiently high MTTFs before the entire drive can be deemed suitable for safety-critical applications. In addition, since high-resolution position sensors have relatively low MTTFs, designers must use risk reduction methods in order to comply with the safety standards. Among possible methods, the use of two or more redundant position sensors is quite common [13]: this, however, increases costs noticeably. Thus, a considerable amount of international research has been performed over the past three decades to find robust and cost-effective replacements for these high-resolution sensors.

One line of investigation is based on the idea of replacing the high-resolution sensors with more rugged, low-resolution position sensing systems [14]–[27]. Among these, binary Hall-effect sensors are the most common and inexpensive [14], costing less than 0.5 € when purchased in bulk. A well-known layout uses

Manuscript received January 3, 2017; revised June 12, 2017, October 11, 2017, and December 24, 2017; accepted March 19, 2018. Date of publication March 26, 2018; date of current version November 19, 2018. Recommended for publication by Associate Editor Prof. J. Hur. *(Corresponding author: Giacomo Scelba.)*

G. De Donato and F. Giulii Capponi are with the Department of Astronautical, Electrical, and Energy Engineering, University of Rome "La Sapienza," Rome 00184, Italy (e-mail: giulio.dedonato@uniroma1.it; fabio.giuliicapponi@uniroma1.it).

G. Scelba and G. Scarcella are with the Department of Electrical, Electronic Engineering, and Computer Science (DIEEI), University of Catania, Catania 95125, Italy (e-mail: giacomo.scelba@dieei.unict.it; giuseppe.scarcella@dieei.unict.it).

M. Pulvirenti was with the Department of Electrical, Electronic Engineering, and Computer Science (DIEEI), University of Catania, Catania 95125, Italy. He is now with the STMicroelectronics, Catania 95121, Italy (e-mail: mario.pulvirenti@dieei.unict.it).

Color versions of one or more of the figures in this paper are available online at http://ieeexplore.ieee.org.

Digital Object Identifier 10.1109/TPEL.2018.2820042

TABLE I
EXAMPLES OF HAZARDOUS EVENTS THAT MAY OCCUR IN A PASSENGER VEHICLE

Hazardous Event	ASIL Level (ISO 26262)	SIL Level (IEC 61508)	Dangerous Failures per Hour
Unintended closing of window lifter [8]	A	1	$10^{-6} \le \text{DFH} < 10^{-5}$ 1/h
Unitended vehicle acceleration during a low speed manoeuvre amongst pedestrians [9]	B	2	$10^{-7} \le \text{DFH} < 10^{-6}$ 1/h
Loss of brake-by-wire braking effect at speeds above 100 km/h [10]	C	2	$10^{-7} \le \text{DFH} < 10^{-6}$ 1/h
Unintended steering assist [11]	D	3	$10^{-8} \le \text{DFH} < 10^{-7}$ 1/h

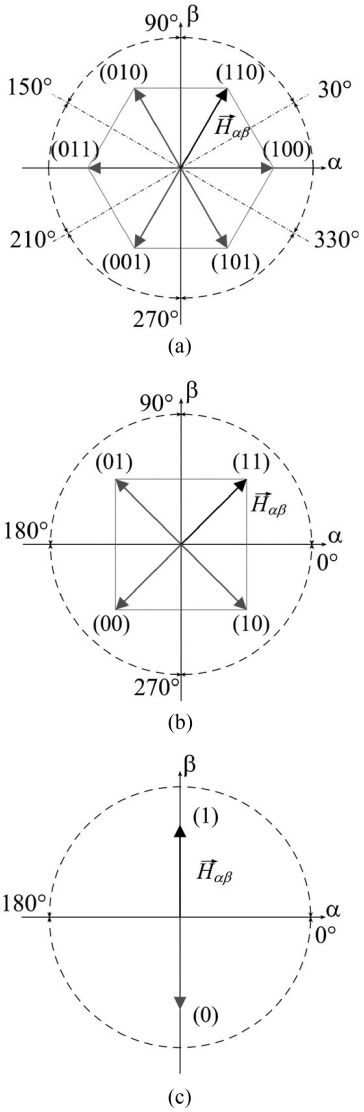

Fig. 1. Quantized rotating position vector $\boldsymbol{H}_{\alpha\beta}$ loci for low-resolution position sensing systems [14]. (a) 3 BPP. (b) 2 BPP. (c) 1 BPP.

three Hall-effect sensors, displaced 120 electrical degrees apart. This layout provides a 60 electrical degree resolution, i.e., 3 BPP, as shown in Fig. 1(a). If only two sensors are used and displaced by 90 electrical degrees, the resolution drops to 90 electrical degrees, i.e., 2 BPP, as shown in Fig. 1(b). The lowest possible resolution, i.e., 180 electrical degrees, or 1 BPP, is obtained when using a single sensor, as shown in Fig. 1(c). In order to obtain high-resolution position and speed estimates from these low-resolution sensing systems, a number of algorithms have been developed [15]–[24]. Recently, it has been demonstrated that the 3 BPP position sensing system, equipped with an appropriate fault detection, identification, and compensation algorithm, possesses an inherent triple modular redundancy to faults, while the 2 BPP sensing system possesses a dual modular redundancy [25], [26]. On the other hand, a key limitation of these sensing systems is that the position sample rate is speed dependent [19]. This results in degraded position and speed estimation at speeds less than about 0.1 p.u. To avoid unstable operation in this speed range, strong filtering in the position and speed estimation algorithms is necessary, leading to reduced performances with respect to medium- to high-speed operation.

A second line of investigation is based on the core idea that the motor itself can be used as a high-resolution position sensor. This has led to the development of a significant number of self-sensing algorithms, able to extract position and speed estimates directly from voltage and/or current measurements [29]–[51]. In the medium- to high-speed range, back electromotive force (EMF) tracking is the de facto industry standard method [29]. This fails at low speeds due to a reduced signal-to-noise ratio, which produces degradation in the quality of the estimates and ultimately causes loss of stability [30]. In this low-speed range, self-sensing strategies based on high-frequency signal injection have been proven to be effective for electromagnetically salient machines. The literature reports high-frequency injection methods for both interior permanent-magnet (IPM) [31]–[46] and surface permanent-magnet (SPM) machines [47]–[52]: for the former, the saliency is produced by the rotor geometry, while for the latter, it is usually due to local saturation in the stator.

In safety-critical systems, self-sensing methods cannot replace the position sensor but can be used as a backup following a position sensor fault, such as in the limp-home mode available in vehicles [53]–[55]. Not only is the use of position sensors mandatory, but also compliance with the required SIL, to keep the risk of dangerous failures below the limits set by the safety standards.

The aim of this paper is to show that binary Hall-effect sensors can be considered as a viable replacement for high-resolution position sensors in PMSM drives requiring up to SIL 3 or ASIL D compliance. Initially, an in-depth investigation of their reliability is performed, together with an analysis of their low-speed limitations. It then is recognized that these may be overcome by merging the sensors' outputs with high-frequency signal

injection, as long as the machine possesses a detectable amount of electromagnetic saliency. In this contribution, the state-of-the-art quantization-harmonic-decoupling vector-tracking observer (VTO) [21], is used for speed and position estimation. It is shown how the algorithm can be integrated with any pulsating or rotating high-frequency signal injection method, with negligible modifications to its structure. Extensive simulation and experimental results are then provided for a 3.7 kW IPM drive using 1, 2, and 3 BPP position sensing systems, in both healthy and faulty conditions.

II. Hall-Effect Position Sensor-Based PMSM Drives

Key aspects related to Hall-effect-position-sensor-based PMSM drives are described in this section. Basic reliability analysis applied to Hall-effect-based position sensing is introduced in Section II-A. Section II-B and II-C describes how the sensors' signals may be processed and fed to a VTO, in order to obtain high-resolution estimates of speed and position. Section II-D describes how the reduced position sample rate at low-speeds degrades the performance of such drives.

A. Reliability of Hall-Effect-Based Position Sensing

From a reliability stand point, Hall-effect sensors behave like any other nonrepairable electronic component. For these, it is possible to define a lifetime *T,* as the amount of time during which the component performs its intended function. By nature, *T* is a continuous random variable with a probability density function *f*(*t*), known as the time to failure distribution [56]. The probability that a nonrepairable component will survive beyond a specified time *t*, $P(T > t)$, is equivalent to its reliability function $R(t)$. This is formally defined in probability theory as a complementary cumulative distribution function

$$R(t) = P(T > t) = \int_t^{+\infty} f(x)dx. \tag{1}$$

The MTTF of a component is defined as the mean value of *T*

$$\mathrm{MTTF} = \int_0^{+\infty} tf(t)dt = \int_0^{+\infty} R(t)dt. \tag{2}$$

Moreover, the failure rate of a component $h(t)$ is defined as the conditional probability that a fault may occur in a time interval *dt*, given that the component has not failed before time *t*. It is formally defined as

$$h(t) = \frac{f(t)}{R(t)} = -\frac{d[\log R(x)]}{dx}. \tag{3}$$

Based on this, it is also possible to express $R(t)$ as

$$R(t) = \exp\left(-\int_0^t h(x)dx\right). \tag{4}$$

When faults due to infant mortality and aging are not taken into account, it is quite common to assign a constant failure rate λ to many components

$$h(t) = \lambda. \tag{5}$$

The failure rate is usually expressed in failures per hour (1/h) or in number of failures every 10^9 h of operation, also known as failures in time (FIT). Specifically, for a Hall-effect sensor, the failure rate may be indicated as λ_{Hall}. Thus, the reliability function for a single Hall-effect sensor becomes an exponential distribution

$$R_{\mathrm{Hall}}(t) = e^{-\lambda_{\mathrm{Hall}}t}. \tag{6}$$

For this distribution, it can easily be calculated that

$$\mathrm{MTTF}_{\mathrm{Hall}} = \frac{1}{\lambda_{\mathrm{Hall}}}. \tag{7}$$

When more than one component is used, particular care must be taken in order to calculate the correct MTTF [57]. For example, when three Hall-effect sensors are used as a 3 BPP sensing system without any fault detection, identification, and compensation algorithm [25], [26], a failure of any one of the three will compromise the entire sensing system. From a reliability-engineering point of view, this corresponds to a series reliability architecture. In this case, the reliability function of the whole sensing system $R_{3\Sigma\mathrm{Hall}}(t)$ is equal to the product of the reliability functions of each sensor

$$R_{3\sum \mathrm{Hall}}(t) = R_{\mathrm{Hall},1}(t)\, R_{\mathrm{Hall},2}(t)\, R_{\mathrm{Hall},3}(t) = R_{\mathrm{Hall}}(t)^3. \tag{8}$$

In (8) and in the following equations, it is assumed that the three sensors have equal reliability functions, i.e., they come from the same production lot. Equation (8) implies that the reliability of the sensing system will be smaller than that of each Hall-effect sensor. It can be calculated that the MTTF for such an arrangement is equal to

$$\mathrm{MTTF}_{3\sum \mathrm{Hall}} = \frac{1}{\sum_{k=1}^{3}\lambda_{\mathrm{Hall},k}} = \frac{1}{3\lambda_{\mathrm{Hall}}} = \frac{1}{3}\mathrm{MTTF}_{\mathrm{Hall}}. \tag{9}$$

The corresponding failure rate can be found from (3), by using $R_{3\Sigma\mathrm{Hall}}(t)$

$$h(t)_{3\sum \mathrm{Hall}} = 3\lambda_{\mathrm{Hall}}. \tag{10}$$

On the other hand, if a fault detection, identification, and compensation algorithm is used, the sensing system possesses a triple modular redundancy and constitutes a parallel reliability architecture. In this case, it can be shown that the reliability function of the sensing system $R_{3//\mathrm{Hall}}(t)$ is equal to

$$R_{3//\mathrm{Hall}}(t) = 1 - [1 - R_{\mathrm{Hall}}(t)]^3. \tag{11}$$

This implies that the reliability of the system will be larger than that of each sensor. It can be calculated that the MTTF for such an arrangement is equal to

$$\mathrm{MTTF}_{3//\mathrm{Hall}} = \frac{1}{\lambda_{\mathrm{Hall}}}\sum_{k=1}^{3}\left(\frac{1}{k}\right) = \frac{11}{6\lambda_{\mathrm{Hall}}} = \frac{11}{6}\mathrm{MTTF}_{\mathrm{Hall}}. \tag{12}$$

By comparing (9) and (12), it can be seen that the MTTF for a 3 BPP position sensing system improves by a factor of 5.5 when a fault detection, identification, and compensation algorithm is used. The failure rate is obtained by substituting $R_{3//\mathrm{Hall}}(t)$

TABLE II
MTTFs AND FITs FOR 3 AND 2 BPP POSITION SENSING SYSTEMS (FOR $\lambda_{\text{HALL}} = 55.5$ FIT AND $T_{\text{MISSION}} = 20$ YEARS)

	Series reliability architecture (i.e. without fault detection, identification and compensation)		Parallel reliability architecture (i.e. with fault detection, identification and compensation)	
	MTTF	Failure Rate	MTTF	Failure Rate
3 BPP position sensing	6 10^6 h	166.5 FIT	3.3 10^7 h	1.55 10^{-2} FIT
2 BPP position sensing	9 10^6 h	111 FIT	2.7 10^7 h	1.07 FIT

into (3)

$$h(t)_{3//\text{Hall}} = \frac{3\lambda_{\text{Hall}} e^{-\lambda_{\text{Hall}} t}\left(1 - e^{-\lambda_{\text{Hall}} t}\right)^2}{1 - \left(1 - e^{-\lambda_{\text{Hall}} t}\right)^3}. \tag{13}$$

$H(t)$ is time dependent and increases monotonically with time; a mission time T_{mission} must be defined to calculate the correct failure rate. Standard values for T_{mission} range from 10 years (87 600 h) to 30 years (262 800 h), depending on the application.

For a 2 BPP sensing system, it can be shown that the MTTFs for the series and parallel reliability architectures are

$$\text{MTTF}_{2\sum \text{Hall}} = \frac{1}{\sum_{k=1}^{2} \lambda_{\text{Hall},k}} = \frac{1}{2\lambda_{\text{Hall}}} = \frac{1}{2}\text{MTTF}_{\text{Hall}} \tag{14}$$

$$\text{MTTF}_{2//\text{Hall}} = \frac{1}{\lambda_{\text{Hall}}} \sum_{k=1}^{2} \left(\frac{1}{k}\right) = \frac{3}{2\lambda_{\text{Hall}}} = \frac{3}{2}\text{MTTF}_{\text{Hall}}. \tag{15}$$

In this case, the MTTF improves by a factor of 3 when fault detection, identification, and compensation is present. The related failure rates are

$$h(t)_{2\sum \text{Hall}} = 2\lambda_{\text{Hall}} \tag{16}$$

$$h(t)_{2//\text{Hall}} = \frac{2\lambda_{\text{Hall}} e^{-\lambda_{\text{Hall}} t}\left(1 - e^{-\lambda_{\text{Hall}} t}\right)}{1 - \left(1 - e^{-\lambda_{\text{Hall}} t}\right)^2}. \tag{17}$$

According to the limited literature available [58]–[60], estimates of Hall-effect sensor MTTFs are in the range of 10^6–10^8 h, with the former value suggested for use in extreme environmental conditions. For example, assuming $\text{MTTF}_{\text{Hall}} = 1.8 \times 10^7$ h and $\lambda_{\text{Hall}} = 55.5$ FIT, as reported in [60], and assuming T_{mission} equal to 20 years (i.e., 175 200 h), Table II reports the MTTFs and failure rates for 3 and 2 BPP position sensing systems, for both series and parallel reliability architectures.

The values reported earlier prove that both 3 BPP and 2 BPP Hall-effect position sensing systems, equipped with a fault detection, identification, and compensation algorithm, have MTTFs and failure rates that are within the required range for use in SIL 3 or ASIL D compliant drives.

B. Quantized Rotating Position Vectors

It was shown in [19] that the information coming from binary Hall-effect sensors can be interpreted as a quantized-rotating position vector $\boldsymbol{H}_{\alpha\beta}$ in the stationary reference plane. Fig. 1 shows the $\boldsymbol{H}_{\alpha\beta}$ loci for the three cases of 3, 2, and 1 BPP resolution. As the rotor rotates, the $\boldsymbol{H}_{\alpha\beta}$ locus forms the vertices of a hexagon in Fig. 1(a), consistent with a 60° spatial resolution. Since $\boldsymbol{H}_{\alpha\beta}$ has six separate positions in the plane, it is also said that such an arrangement has number of discrete states, N_{DS}, equal to 6. For a 90° resolution, the locus forms the vertices of a square, as shown in Fig. 1(b), so $N_{\text{DS}} = 4$. This is the lowest possible resolution, from which it is possible to detect the rotor's direction of rotation [23]. As a visual proof of this, Fig. 1(c) shows how the locus collapses to the β axis when the position sensing system has only 1 BPP, i.e., $N_{\text{DS}} = 1$. In this case, $\boldsymbol{H}_{\alpha\beta}$ simply switches back and forth along the axis and no information about the direction of rotation is available.

$\boldsymbol{H}_{\alpha\beta}$ can be decomposed into a spatial Fourier series of continuously rotating harmonic vectors [20]. The general formulation, for any value of N_{DS}, was derived in [21]

$$\boldsymbol{H}_{\boldsymbol{\alpha\beta}} = e^{j\left(\theta_{re\_\text{Hall}} - \frac{\pi}{N_{\text{DS}}}\right)} + \sum_{k=1}^{+\infty} \times \left[-\frac{1}{N_{\text{DS}}k - 1} e^{-j\left((N_{\text{DS}}k-1)\theta_{re\_\text{Hall}} + \frac{\pi}{N_{\text{DS}}}\right)} + \frac{1}{N_{\text{DS}}k + 1} e^{j\left((N_{\text{DS}}k+1)\theta_{re\_\text{Hall}} - \frac{\pi}{N_{\text{DS}}}\right)} \right] \tag{18}$$

where $\theta_{\text{re\_Hall}}$ is the electrical angle of the fundamental rotating vector.

It can be seen in (18) that there are both positively and negatively rotating harmonic vectors. It can also be noted that the number, order, and amplitude of the harmonic vectors depend on N_{DS}. In the case of $N_{\text{DS}} = 6$, i.e., BPP $= 3$, the first-order ($k = 1$) harmonic vectors are the negatively rotating fifth and positively rotating seventh. The frequencies of higher order harmonic vectors are separated by six times the fundamental frequency. For $N_{\text{DS}} = 4$, i.e., BPP $= 2$, the first-order harmonic vectors are the negatively rotating third and positively rotating fifth. Higher order harmonic vectors are spaced apart by four times the fundamental frequency. For $N_{\text{DS}} = 2$, i.e., BPP $= 1$, the first-order harmonic vectors are the negatively rotating first and positively rotating second. Higher order harmonic vectors are spaced apart by the fundamental frequency.

Hence, the frequency separation between harmonic vectors depends on both the number of discrete states of the sensing system and on the rotor's frequency of rotation. This is due to the fact that the sampling rate of the position measurement f_{s_Hall} is speed dependent

$$f_{s\_\text{Hall}} = N_{\text{DS}} P \frac{\omega_r}{2\pi} \tag{19}$$

where P is the number of pole pairs and ω_r is the rotor speed. Thus, as the speed drops, the position-sampling rate decreases and the quantization harmonics become more tightly spaced in

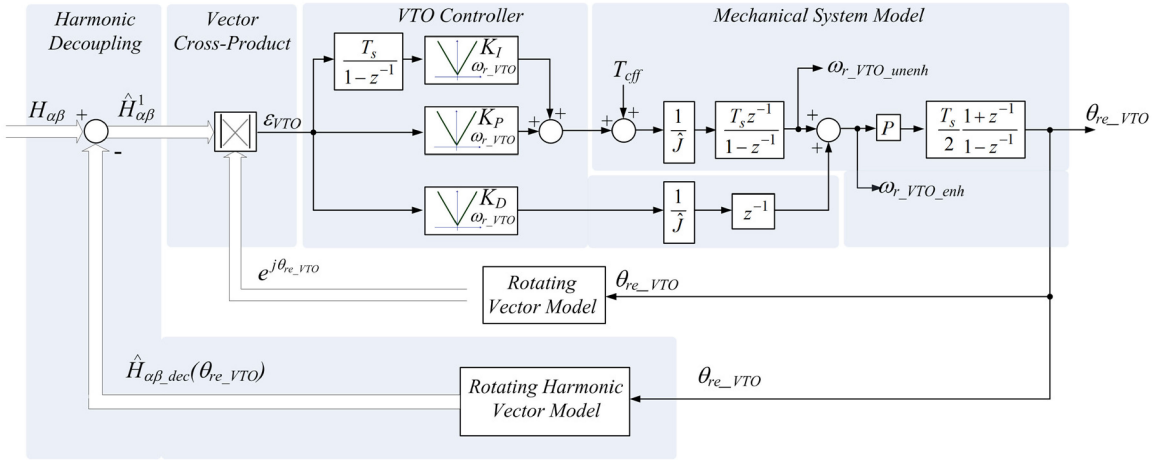

Fig. 2. Quantization-harmonic-decoupling VTO [21].

the frequency domain, making it more difficult to filter them out. This effect degrades the low-speed performance of any low-resolution sensor-based PMSM drive.

C. Quantization Harmonic Decoupling

By using harmonic decoupling, it is possible to extract the fundamental-harmonic rotating vector, which contains the sought-after high-resolution information. The higher order harmonic vectors are removed from $\mathrm{H}_{\alpha\beta}$ by subtracting $\mathrm{H}_{\alpha\beta\_\mathrm{dec}}$, defined as

$$\boldsymbol{H}_{\alpha\beta\_\mathrm{dec}} = \boldsymbol{H}_{\alpha\beta} - e^{j(\theta_{re\_\mathrm{Hall}} - \pi/6)}. \tag{20}$$

Fig. 2 shows how this is achieved in a quantization-harmonic-decoupling VTO, i.e., a Luenberger-style observer in which vector cross-product phase detection is used together with quantization-harmonic vector decoupling. When the VTO is locked, the output of the phase detector can be approximated as

$$\varepsilon_{\mathrm{VTO}} = \sin\left(\Delta\theta_{re\_\mathrm{Hall}}\right) \approx \Delta\theta_{re\_\mathrm{Hall}} = \hat{\theta}_{re\_\mathrm{Hall}} - \theta_{re\_\mathrm{VTO}} \tag{21}$$

where $\hat{\theta}_{re\_\mathrm{Hall}}$ is the phase of the decoupled, fundamental-harmonic rotating vector and θ_{re_VTO} is the position estimate of the VTO. An accurate estimate of the accelerating torque T_{cff} allows θ_{re_VTO} to have virtually zero-lag and extends the estimation bandwidth well above the bandwidth due to the VTO controller alone. Furthermore, within the estimation bandwidth, the parameter (inertia) error sensitivity on the estimation accuracy is very limited, as shown in [28]. A zero-lag θ_{re_VTO} is also very helpful in achieving precise quantization-harmonic decoupling.

D. Low-Speed Limitations

Unfortunately, at very low speeds the filtering effect of the moment of inertia is felt little, so even small errors in the instantaneous estimation of T_{cff} will cause both the speed and position estimates to deviate from the actual values. This in turn causes nonideal harmonic decoupling, i.e., $\hat{\boldsymbol{H}}_{\alpha\beta\_\mathrm{dec}}(\theta_{re\_\mathrm{VTO}})$ is no longer equal to $\mathrm{H}_{\alpha\beta\_\mathrm{dec}}$. Furthermore, due to the reduced value of f_{s_Hall}, any quantization harmonic noise that is not removed by the decoupling is also poorly filtered by the VTO controller and tends to propagate, causing undesired ripple both in the speed and position estimates. This, in turn, degrades the torque and speed control of the drive. Fig. 3 shows this effect experimentally on a speed-controlled PMSM drive, whose ratings are reported in Section V. The resolution of the position measurement is equal to 60° and the VTO is tuned to have a 20 Hz bandwidth. T_{cff} is obtained by multiplying the measured q-axis current, i_q, by the torque constant of the machine. Initially, the motor rotates at 20 rad/s in steady state, but when the speed is reduced to 3 rad/s, quantization-harmonic-induced ripple appears in the speed and position estimates due to incorrect harmonic decoupling, causing significant oscillations in the actual speed of rotation.

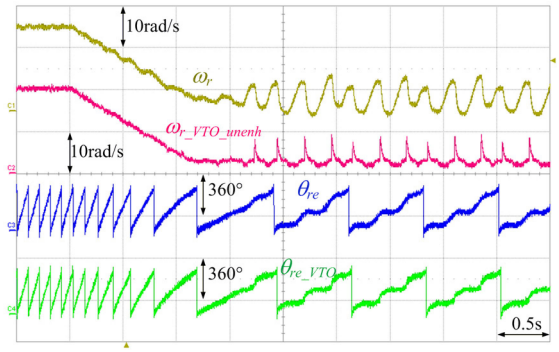

Fig. 3. Low-speed transient from 20 to 3 rad/s for a 3 BPP sensing system. The VTO is tuned for a 20 Hz bandwidth.

To reduce this effect, in [21], it was proposed to reduce the observer bandwidth at low speeds, i.e., to make the VTO controller gains speed dependent. This can be seen in Fig. 2, where the gains are linear functions of the estimated speed; usually the unenhanced speed estimate $\omega_{r\_\mathrm{VTO\_unenh}}$ is used, since it is more filtered compared to the enhanced estimate $\omega_{r\_\mathrm{VTO\_enh}}$. As a rule of thumb, the minimum value of the VTO controller gains can

be set to 5%–10% of their nominal values. The observer bandwidth f_{BW} should be increased as the speed of rotation increases, up to a limit speed ω_{r_lim} above which the rated bandwidth is reached

$$\omega_{r\_\mathrm{lim}} = \frac{2\pi f_{\mathrm{BW}}\,\mathrm{SR}}{\mathrm{PN_{DS}}} \tag{22}$$

$$\mathrm{SR} = \frac{f_s}{f_{\mathrm{BW}}} \tag{23}$$

with SR being the sampling ratio between the position sampling frequency and the observer bandwidth. The lowest value of SR is 2, as dictated by the Nyquist–Shannon sampling theorem; usually, SR is chosen to be greater than 2, to guarantee sufficient noise filtering by the VTO. The specific value to be used depends on the attainable accuracy of T_{cff}. It is clear that such a solution adversely affects the dynamic response of the drive at low speed.

III. Flux-Deviation-Based High-Frequency Signal Injection Technique

The only way to overcome the low-speed limitation described earlier is to exploit any additional high-resolution rotor position information that can be obtained. If the machine possesses some electromagnetic saliency, then this can be detected through the injection of additional high-frequency fields and may be used to aid position and speed estimation. In order to be a viable solution, such an additional injection should come at no additional cost, and both the injection procedure and demodulation algorithm should use the existing hardware only. While in principle this approach will work for synchronous reluctance machines as well, in this paper it is proposed and validated for PMSM machines alone.

Among possible saliency-detection algorithms, the flux-deviation-based pulsating injection technique [31] can be used to evaluate any misalignment $\Delta\theta_{re\_\mathrm{HF}}$ between the actual and the estimated rotor positions. By injecting a sinusoidally time-varying voltage signal v_{HF} at a high frequency ω_{HF} along a fixed arbitrary direction d' (24), a corresponding magnetomotive force F_{HF} is generated in the air gap, as shown in Fig. 4(a). F_{HF} is spatially in phase with the flux linkage λ_{HF} only if v_{HF} is injected along the direction of the true d- or q-axes. In all the other cases, a flux linkage component $\lambda_{q'\mathrm{HF}}$ arises on the q'-axis orthogonal to the high-frequency injection d'-axis. Thus, a q'-axis high-frequency back EMF $e_{q'\mathrm{HF}}$ is induced, causing the flow of a high-frequency current $i_{q'\mathrm{HF}}$. As shown in Fig. 4(a), the amplitudes of these induced signals are modulated by the misalignment $\Delta\theta_{re\_\mathrm{HF}}$ between the d'- and d-axes. In particular, $\lambda_{q'\mathrm{HF}}$ and $e_{q'\mathrm{HF}}$ approach zero anytime the d'-axis of injection coincides with the true d- or q-axes. Naturally, this amplitude modulation arises only if a saliency is present, i.e., when the high-frequency d-axis inductance $L_{d\mathrm{HF}}$ differs from the high-frequency q-axis inductance $L_{q\mathrm{HF}}$. It can be shown that the low-frequency envelope ζ_{HF} of $i_{q'\mathrm{HF}}$ is proportional to the sine of $2\Delta\theta_{re\_\mathrm{HF}}$ (25), in which L_{diff} is the differential high-frequency

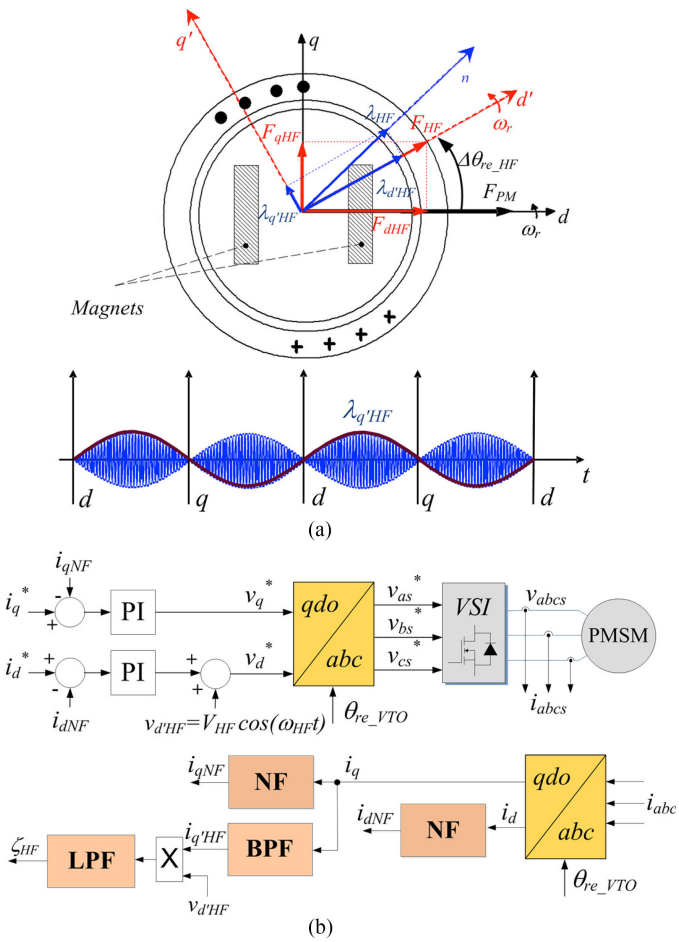

Fig. 4. Flux-deviation-based pulsating injection technique. (a) HF space vector diagram. (b) Practical implementation.

inductance, as defined in (26)

$$v_{\mathrm{HF}} = [v_{q'\mathrm{HF}}; v_{d'\mathrm{HF}}] = [0; V_m \cos(\omega_{\mathrm{HF}} t)] \tag{24}$$

$$\zeta_{\mathrm{HF}} = -\frac{v_{d'\mathrm{HF}}}{2\omega_{\mathrm{HF}}} \frac{L_{\mathrm{diff}}}{L_{d\mathrm{HF}} L_{q\mathrm{HF}}} \sin(2\Delta\theta_{re\_\mathrm{HF}}) \tag{25}$$

$$L_{\mathrm{diff}} = \frac{L_{q\mathrm{HF}} - L_{d\mathrm{HF}}}{2}. \tag{26}$$

ζ_{HF} can be obtained in practice by performing a demodulation of $i_{q'\mathrm{HF}}$. A simple and well-known method to achieve this is shown in Fig. 4(b), in which $i_{q'\mathrm{HF}}$ is firstly isolated from the fundamental current through a bandpass filter (BPF); ζ_{HF} is then obtained by multiplying $i_{q'\mathrm{HF}}$ by a sinusoidal signal at the carrier frequency and by then applying a low-pass filter. No additional hardware is required. Notch filters (NF) remove the high-frequency component from the feedback. The reference frame transformations are performed by using θ_{re_VTO}, meaning that the misalignment between the d- and d'-axes is equal to

$$\Delta\theta_{re\_\mathrm{HF}} = \theta_{re\_\mathrm{VTO}} - \theta_{re\_\mathrm{HF}} \tag{27}$$

with θ_{re_HF} the position of the true d-axis, as sensed via the high-frequency injection.

IV. Signal-Injection-Aided Position and Speed Estimation

A theoretical analysis of the signal-injection-aided VTO is performed in Section IV-A. The operating point models are derived, highlighting some key aspects that arise in speed and position estimation due to the merging of self-sensing with Hall-effect sensors. Section IV-B reports simulations of the drive in the low-speed range, comparing performances both without and with the signal-injection aid. In Section IV-C, Hall-effect sensor faults at low speeds are simulated in order to investigate how the signal-injection-aided VTO-based drive compares to the standard VTO-based drive in faulty conditions.

A. Operating Point Analysis

By comparing (21) and (25), it can be noted that ζ_{HF} has the same nature as $\varepsilon_{\mathrm{VTO}}$. The core idea of this paper is to blend these signals together in the simplest possible way, to improve the low-speed performance of the quantization-harmonic decoupling VTO. This can be done if both signals have the same units, so ζ_{HF} must be multiplied by

$$K_{\mathrm{HF}} = \frac{\omega_{\mathrm{HF}}}{v_{d'\mathrm{HF}}} \frac{L_{d\mathrm{HF}} L_{q\mathrm{HF}}}{L_{\mathrm{diff}}} \tag{28}$$

so that an error $\varepsilon_{\mathrm{HF}}$ results

$$\varepsilon_{\mathrm{HF}} = K_{\mathrm{HF}} \zeta_{\mathrm{HF}} = -\frac{1}{2} \sin\left(2\Delta\theta_{re\_\mathrm{HF}}\right) \tag{29}$$

if $\Delta\theta_{re\_\mathrm{HF}}$ is small, then

$$\varepsilon_{\mathrm{HF}} \approx -\Delta\theta_{re\_\mathrm{HF}}. \tag{30}$$

Subtracting $\varepsilon_{\mathrm{VTO}}$ and $\varepsilon_{\mathrm{HF}}$ results in the following:

$$\begin{aligned} \varepsilon_{\mathrm{VTO}} - \varepsilon_{\mathrm{HF}} &\approx \left(\hat{\theta}_{re\_\mathrm{Hall}} - \theta_{re\_\mathrm{VTO}}\right) - \left(\theta_{re\_\mathrm{HF}} - \theta_{re\_\mathrm{VTO}}\right) \\ &= \hat{\theta}_{re\_\mathrm{Hall}} - \theta_{re\_\mathrm{HF}}. \end{aligned} \tag{31}$$

The difference between $\varepsilon_{\mathrm{VTO}}$ and $\varepsilon_{\mathrm{HF}}$ is therefore equal to the difference between the phase of the decoupled fundamental vector and the true d axis, as sensed via the high-frequency signal injection.

Consequently, the VTO should be modified as shown in Fig. 5(a). Compared to Fig. 2, an additional path is present, comprising the high-frequency signal injection, the demodulation process and the subtraction of $\varepsilon_{\mathrm{HF}}$ with $\varepsilon_{\mathrm{VTO}}$. The flux deviation technique is represented in this figure, since it is the technique used in this research; however, any state-of-the-art, pulsating or rotating signal injection method may be used in its place without altering the structure, as long as K_{HF} is consistent. In the figure, the estimated value of K_{HF} is indicated as a function of i_d and i_q. This is because, K_{HF} as well as the position of the true d-axis sensed by the high-frequency injection θ_{re_HF} are the functions of $L_{d\mathrm{HF}}$ and $L_{q\mathrm{HF}}$; as a consequence, they may vary due to magnetic saturation. The extent of such variations is machine dependent. These issues have been comprehensively examined in previous literature [39]–[44], in which lookup tables, structured neural networks, nonlinear adaptive decoupling schemes, and other methods have been proposed. These methods all require some form of self-commissioning procedures to map K_{HF} as a function of i_d and i_q.

Fig. 5(b) shows the signal-injection-aided VTO's operating point model. Ideal quantization harmonic decoupling is assumed, so that $\hat{\theta}_{re\_\mathrm{Hall}}$ represents the angular position of the fundamental rotating vector. The high-frequency signal injection and demodulation technique is modeled as an equivalent low pass filter transfer function $\mathrm{LPF}_{\mathrm{equiv}}(z)$, the input of which is $-\Delta\theta_{re\_\mathrm{HF}}$, with the negative sign required for consistency with (30). The actual transfer function depends on the specific injection and demodulation technique that is used [37]. By applying some simple arithmetic manipulations, the operating point model becomes the one shown in Fig. 5(c). Here, the signal injection correction is shown in terms of θ_{re_VTO} and θ_{re_HF}, separately. θ_{re_VTO} is now fed back to the input thorough $1 - \mathrm{LPF}_{\mathrm{equiv}}(z)$; this means that within the signal injection and demodulation bandwidth, i.e., as long as $\mathrm{LPF}_{\mathrm{equiv}}(z) \approx 1$, θ_{re_VTO} is removed from the feedback. Conversely, θ_{re_HF} is fed back to the input through $\mathrm{LPF}_{\mathrm{equiv}}(z)$; this means that within the signal injection and demodulation bandwidth, θ_{re_HF} acts as the signal-injection-aided VTO's feedback. Assuming $\mathrm{LPF}_{\mathrm{equiv}}(z) \approx 1$, Fig. 5(d) shows the resulting operating point model, which is also consistent with (31).

Outside the bandwidth of the signal injection and demodulation technique, the correct operating point model is the one shown in Fig. 5(c), which indicates that the error signal feeding the VTO controller is no longer precisely equal to (31) and the tracking will deteriorate. Generally speaking, in order to increase the bandwidth of the signal injection method it is necessary to increase the injection frequency [37].

B. Low-Speed-Range Simulations

Simulations have been performed with Simulink to verify the performance of the signal-injection-aided VTO in the low-speed range. An IPM motor drive with the same rated values as the one used in the experimental tests was simulated. Fig. 6 shows the simulated behavior of the drive during the same low-speed transient reported in Fig. 3. No gain scheduling is implemented to reduce the VTO bandwidth at low speeds. Initially, the measured speed and position show oscillations, which are damped out as soon as the high-frequency injection aid becomes active. Fig. 7 shows the observer input errors, $\varepsilon_{\mathrm{VTO}}$, $\varepsilon_{\mathrm{HF}}$, and $\varepsilon_{\mathrm{VTO}} - \varepsilon_{\mathrm{HF}}$, immediately before and after the transition. The visible spikes are produced by the Hall-effect sensor transitions and by the harmonic decoupling, as explained in [21]. It is very insightful to compare $\varepsilon_{\mathrm{VTO}}$ with $\varepsilon_{\mathrm{HF}}$. The former is nonzero only when the information coming from the low-resolution Hall-effect sensors is observable [22]; conversely, the latter is continuously active due to its inherently high-resolution nature, and, as explained earlier, is instrumental in forcing the VTO to track the speed and position states with very limited errors, as shown in Fig. 8. These results prove that the use of signal injection overcomes the limitations described in Section II-D and allows to maintain constant VTO gains throughout the entire speed range.

Signal injection is useful until f_{s_Hall} is sufficiently high to guarantee proper operation of the VTO with the low-resolution

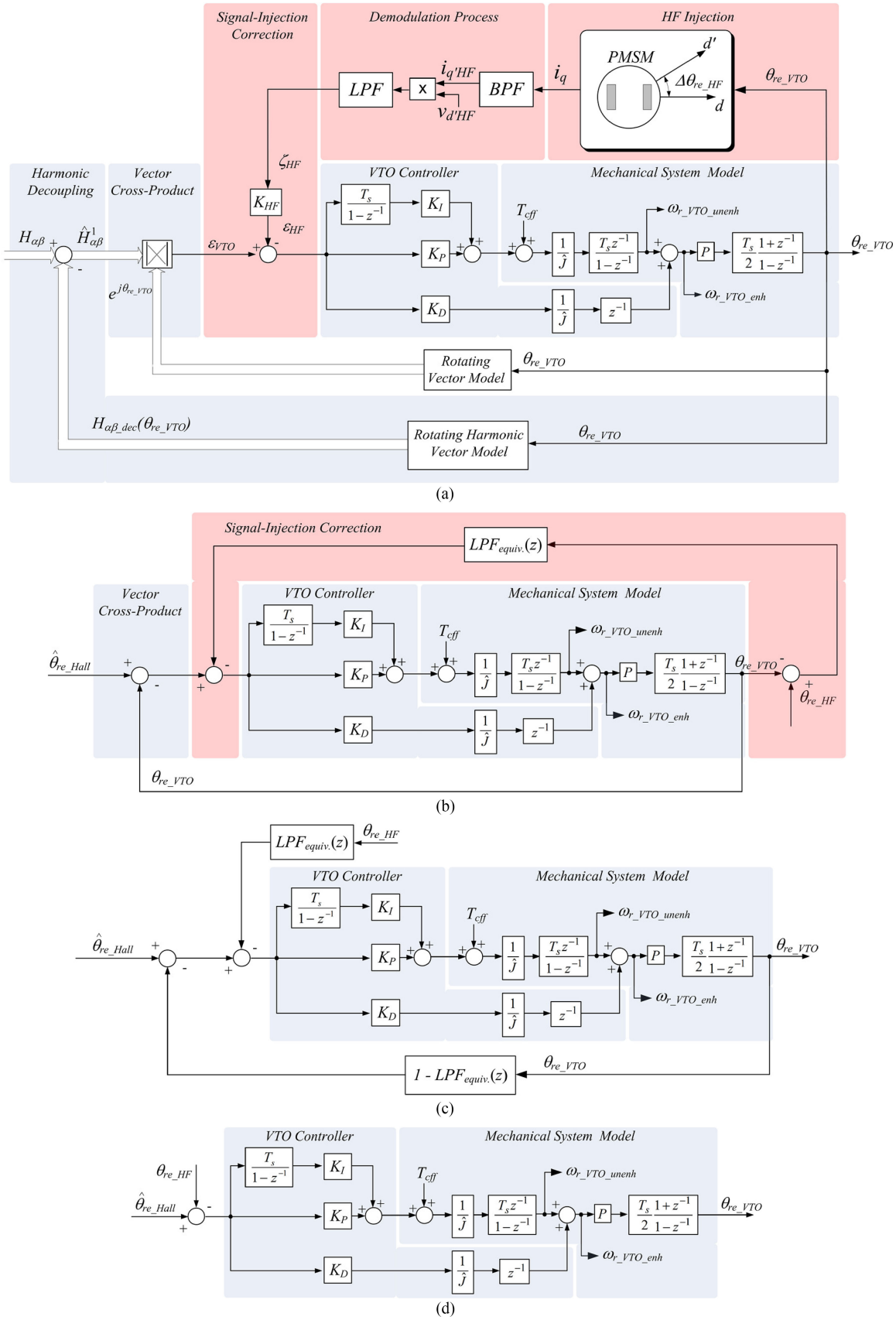

Fig. 5. Signal-injection-aided quantization-harmonic decoupling VTO. (a) Block diagram. (b) Operating point model. (c) Equivalent operating point model. (d) Simplified operating point model, assuming $\mathrm{LPF}_{\mathrm{equiv}}(z) \approx 1$.

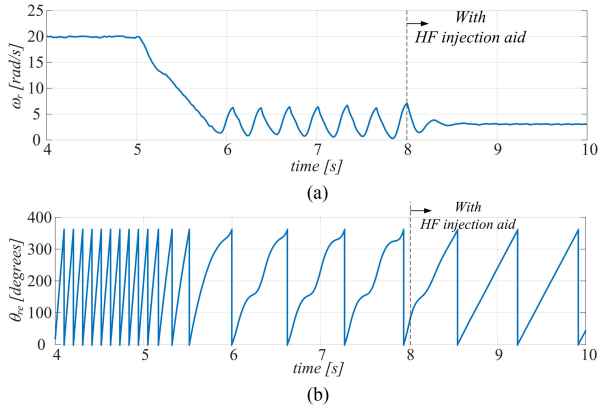

Fig. 6. Simulated low-speed transient from 20 to 3 rad/s for a 3 BPP sensing system. (a) Speed. (b) Angular position.

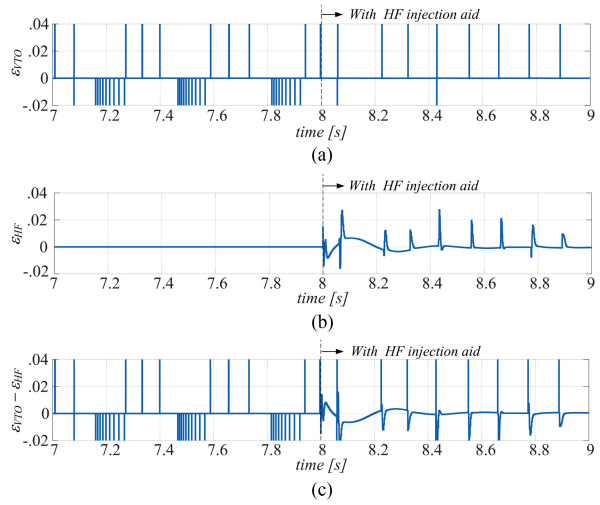

Fig. 7. Simulated low-speed transient from 20 to 3 rad/s for a 3 BPP sensing system. (a) $\varepsilon_{\mathrm{VTO}}$ waveform. (b) $\varepsilon_{\mathrm{HF}}$ waveform. (c) $\varepsilon_{\mathrm{VTO}} - \varepsilon_{\mathrm{HF}}$ waveform.

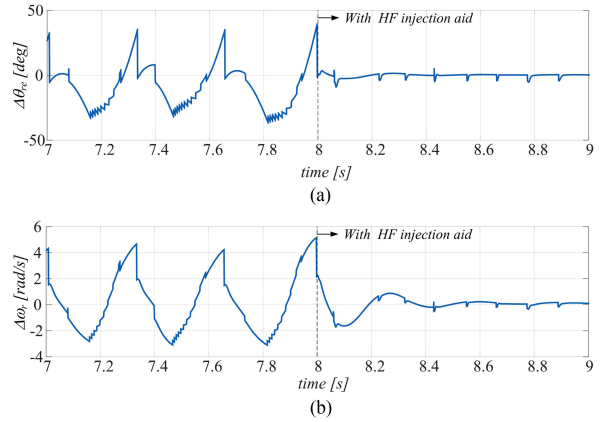

Fig. 8. Simulated low-speed transient from 20 to 3 rad/s for a 3 BPP sensing system. (a) Position estimation error. (b) Speed estimation error.

sensors alone. Thus, above the speed calculated by (22), it is possible to simply deactivate the high-frequency injection by setting $\varepsilon_{\mathrm{HF}} = 0$. For example, in the case of a 3 BPP resolution, 3 pole pairs, 20 Hz VTO bandwidth, the lowest mechanical speed at which the transition can be performed, i.e., for SR $= 2$,

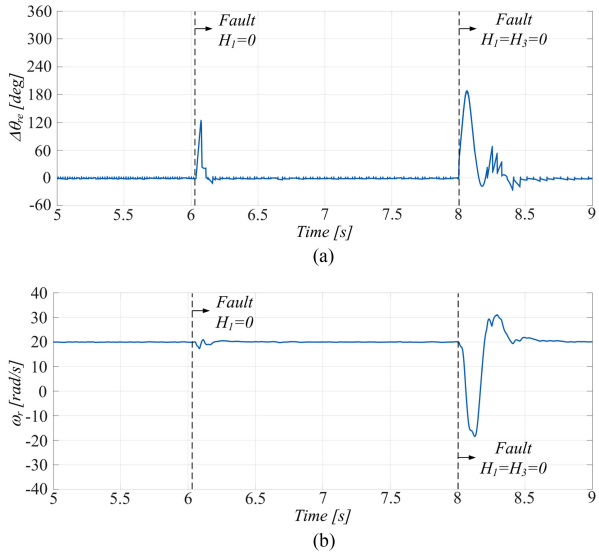

Fig. 9. Simulated low-speed Hall-effect sensor fault transients without signal injection. (a) Position estimation error. (b) Speed estimation error.

is 14 rad/s. It is also possible to execute a smooth transition by implementing a speed-dependent linear combination of $\varepsilon_{\mathrm{HF}}$ and $\varepsilon_{\mathrm{VTO}}$ between minimum and maximum speed thresholds. Such a solution has already been proposed in the literature for transitions between signal-injection and back-EMF based self-sensing [46], [49] and will not be explored further here.

C. Hall-Effect Sensor Fault Simulations

Simulations have also been performed to evaluate the performance of the position sensing system following sensor faults at low speeds. To this end, a 3 BPP system has been used, as it possesses triple modular redundancy. The fault detection, identification, and compensation algorithm described in [25] was used. A single fault is detected when the zero $H_{\alpha\beta}$ vector is measured, i.e., when all of the three sensor signals become 1 or 0. Fault identification occurs at the following sensor state transition, allowing to pinpoint the faulty sensor and the fault type. This is achieved within 360° electrical from the occurrence of the fault. Compensation is then performed by suitably re-adapting the quantization harmonic decoupling. At low speeds, this can mean that a considerable amount of time has to elapse between the occurrence fault and the compensation in the VTO, leading to large position and speed estimation errors and, consequently, oscillatory operation of the drive. This behavior is visible in Fig. 9, which shows the performance of the drive following two successive faults when the speed command is equal to 20 rad/s. For this simulation, no signal injection was used. It can be seen in Fig. 9(a) that the position estimation error reaches 120° electrical in the first post-fault transient and 180° in the second. In addition, Fig. 9(b) shows how the shaft undergoes considerable oscillations following the second fault, before fault compensation is obtained. Conversely, Fig. 10 shows a significantly improved performance following the same faults when the signal-injection-aided VTO is used. Due to the contribution coming from the signal injection, the drive maintains stable

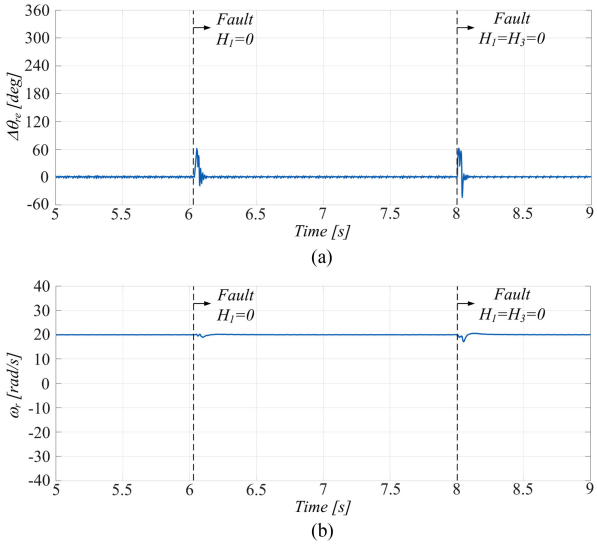

Fig. 10. Simulated during low-speed Hall-effect sensor fault transients with signal injection. (a) Position estimation error. (b) Speed estimation error.

TABLE III
PMSM NAMEPLATE DATA

Rated Power	3.7 kW	Rated Current	6.8 A
Rated Torque	20.2 Nm	Rs	1.8 Ω
Rated Speed	1750 rpm	Lq	0.0377 H
Rated Supply Frequency	87.5 Hz	Ld	0.0329 H
Rated Voltage	369 V	Pole Pairs	3

operation and both faults are identified and compensated faster, since the shaft is able to maintain a smoother speed of rotation. It should be noted that this algorithm is not able to detect failures in the current sensors, which are required for HF injection; a separate fault detection algorithm is necessary for this.

V. EXPERIMENTAL TESTS

The performance of the signal-injection-aided quantization-harmonic decoupling VTO has been evaluated on a three-phase PMSM drive, whose motor specifications are listed in Table III. The position and speed estimation algorithm, the injection and demodulation algorithms and the field-oriented control have been implemented in a single prototyping controller board. The speed control bandwidth of the drive is set to 15 Hz. The unenhanced VTO speed estimate $\omega_{r\_\mathrm{VTO\_unenh}}$ is used for speed feedback. The current control bandwidth is set to 200 Hz. Three low-resolution position sensing systems with 3, 2, and 1 BPP have been emulated by downsampling the output of a 4096 pulse per revolution optical incremental encoder. The signal-injection amplitude and frequency have been set to 25 V and 500 Hz, respectively, for all tests. The demodulation algorithm uses a 200 Hz bandwidth, fourth-order Butterworth BPF centred at 500 Hz and a second-order Butterworth low-pass filter, with a 500 Hz cutoff frequency. The electrical angular position θ_{re} and the mechanical speed ω_r measured by the encoder are shown in the following figures for comparison.

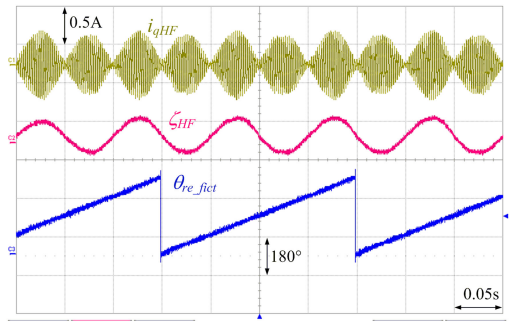

Fig. 11. Blocked rotor no-load high-frequency pulsating signal-injection test.

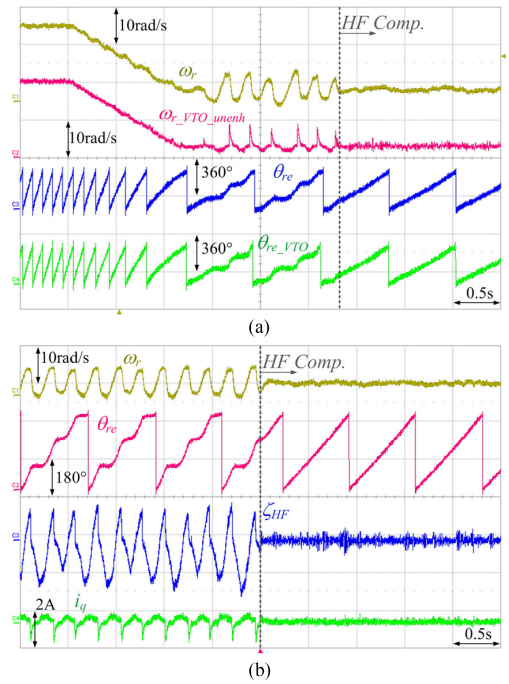

Fig. 12. Low speed behavior when the drive is equipped with a 3 BPP position sensing system and the VTO is tuned for a 20 Hz bandwidth. (a) Transient from 20 to 3 rad/s. (b) Operation for reference speed set to 3 rad/s.

A. No-Load Tests

This section is devoted to tests that have been carried out at no load, i.e., with a disconnected shaft. An initial blocked-rotor test has been performed to measure the degree of electromagnetic saliency of the machine. In this test, only the pulsating high-frequency magnetic field has been injected into the machine and its axis of injection is slowly rotated. Fig. 11 shows some key waveforms recorded during the test: the high-frequency current $i_{q\mathrm{HF}}$, the demodulated saliency signal ζ_{HF}, and the fictitious angle used to rotate the injection axis $\theta_{re\_\mathrm{fict}}$, which is fed to the reference frame transformation of the current control loops. This test has allowed to identify the high-frequency inductances $L_{d\mathrm{HF}} = 33.4\,\mathrm{mH}$, $L_{q\mathrm{HF}} = 54\,\mathrm{mH}$ and thus determine $K_{\mathrm{HF}} = 23.84$. Load tests have shown that the high-frequency inductances tend to remain quite constant throughout the entire operating range, so K_{HF} is maintained equal to the no load value for all of the experimental tests. Fig. 12(a) shows the experimental equivalent of the no-load test shown in Fig. 7, in

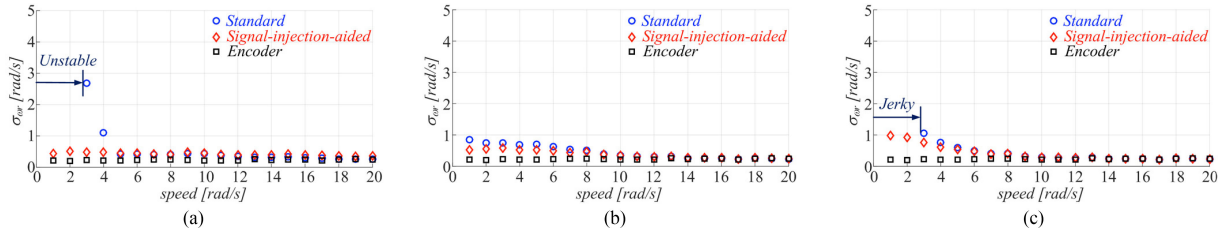

Fig. 13. Standard deviation versus speed reference for a 3 BPP position sensing system, for VTO bandwidths equal to (a) 20 Hz, (b) 10 Hz, and (c) 5 Hz.

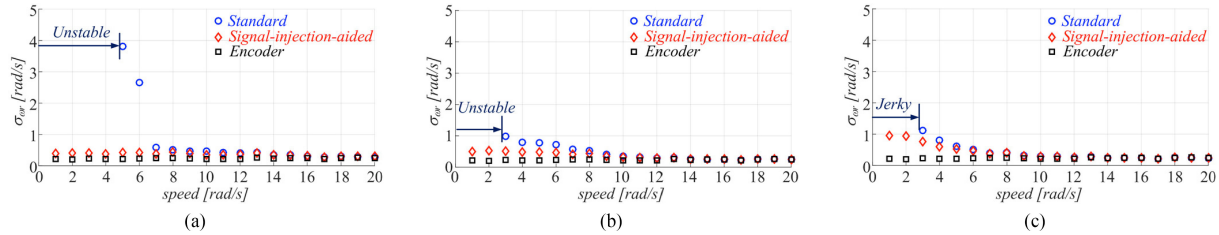

Fig. 14. Standard deviation versus speed reference for a 2 BPP position sensing system, for VTO bandwidths equal to (a) 20 Hz, (b) 10 Hz, and (c) 5 Hz.

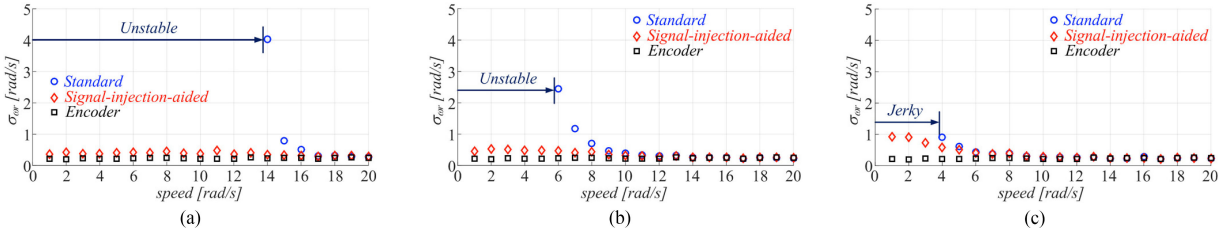

Fig. 15. Standard deviation versus speed reference for a 1 BPP position sensing system, for VTO bandwidths equal to (a) 20 Hz, (b) 10 Hz, and (c) 5 Hz.

which the signal-injection-aided VTO is activated at 3 rad/s, after some time. As expected, the ripple in both rotor position and speed is significantly mitigated once the signal injection is activated. Fig. 12(b) shows another transition from a standard VTO to a signal-injection-aided VTO, with the high-frequency signal injection active throughout the test, but initially not fed to the VTO. Here ζ_{HF} and i_q are also shown, demonstrating how the signal injection tracking is stabilized and the torque ripple is reduced as soon as the signal injection is activated. In order to evaluate the steady state performance of the drive, tests have been executed with the speed reference set to a constant value. The standard deviation of the measured speed $\sigma_{\omega r}$ has been recorded. $\sigma_{\omega r}$ is used as a measure of the speed ripple and of the ability of the drive to track the commanded speed. These tests have been performed at speeds from 20 rad/s down to 1 rad/s, for 3, 2, and 1 BPP resolutions, with standard and signal-injection-aided VTOs, and for observer bandwidths equal to 20, 10, and 5 Hz. Results for the high-resolution encoder-based drive are also reported for comparison. Fig. 13 shows the results related to a 3 BPP resolution. Fig. 13(a) compares $\sigma_{\omega r}$ for the drive operating with 20 Hz bandwidth VTOs; the results obtained when using the standard and signal-injection-aided VTO-based drives, compared to the high-resolution encoder-based drive. Below 5 rad/s, $\sigma_{\omega r}$ is considerably reduced for the signal-injection-aided VTO-based drive; at 3 rad/s, $\sigma_{\omega r}$ is only 18% of that for the standard VTO-based drive, indicating a very strong improvement in speed command tracking when signal-injection is present. Below 3 rad/s the drive without signal injection is unstable, and therefore, it has not been possible to measure $\sigma_{\omega r}$. Conversely, the drive using the signal-injection-aided VTO operates stably at all speeds, with values of $\sigma_{\omega r}$ comparable to those of the high-resolution encoder. Fig. 13(b) reports the same results when the VTO bandwidth is equal to 10 Hz. Compared to Fig. 13(a), it can be seen that no instability occurs, due to the stronger filtering provided by the VTO. For example, at 3 rad/s, $\sigma_{\omega r}$ for the signal-injection-aided drive is 80% of that for the standard VTO-based drive. Fig. 13(c) reports the same results when the VTO bandwidth is equal to 5 Hz. At 3 rad/s, $\sigma_{\omega r}$ for the signal-injection-aided drive is 72% of that for the standard VTO-based drive. Furthermore, below 3 rad/s, the drive using the standard VTO is jerky, but not unstable. This performance degradation

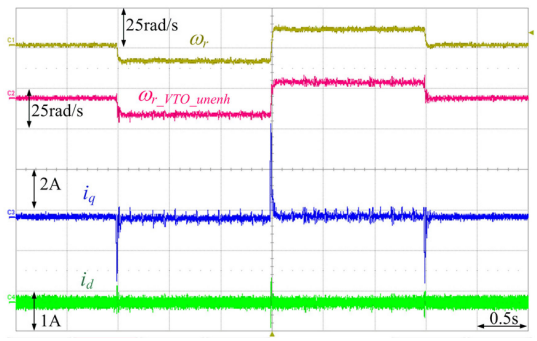

Fig. 16. Low-speed no-load command tracking when the drive is equipped with a 1 BPP position sensing system.

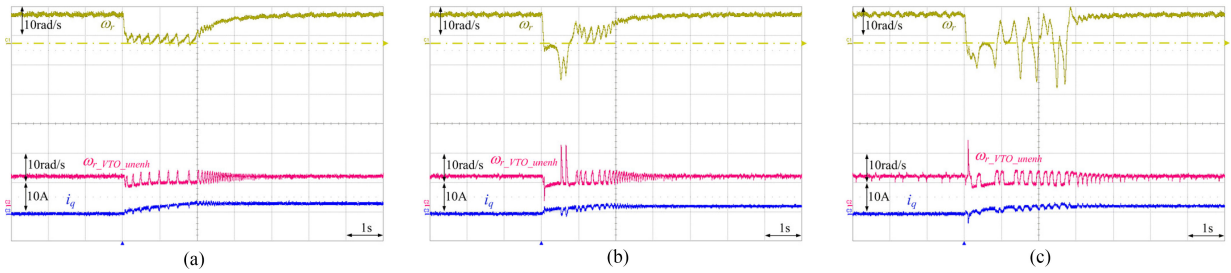

Fig. 17. Disturbance response transient following a 0.4 p.u. step load at 10 rad/s, without signal injection. (a) 3 BPP. (b) 2 BPP. (c) 1 BPP.

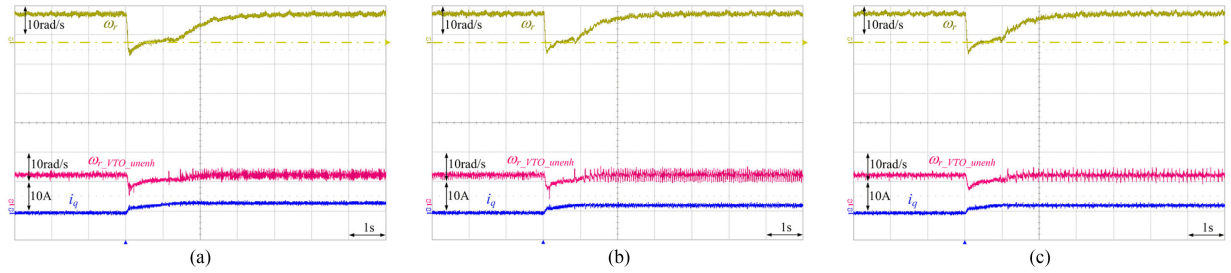

Fig. 18. Disturbance response transient following a 0.4 p.u. step load at 10 rad/s, with signal injection. (a) 3 BPP. (b) 2 BPP. (c) 1 BPP.

compared to Fig. 13(b) is caused by poor speed regulation due to the strongly filtered estimates provided by the VTO. Figs. 14 and 15 report the results for a 2 BPP and a 1 BPP resolution sensing system respectively. It can be seen that instability occurs in a progressively wider speed range, when signal-injection is not used: below 5 rad/s for the 2 BPP system and below 14 rad/s for the 1 BPP system. Furthermore, the low-speed performance of the standard drive, when operating close to its stability limits, is further degraded compared to the 3 BPP case. Fig. 14(a) shows that $\sigma_{\omega r}$ for the signal-injection-aided drive is a 10.9% of that for the standard VTO-based drive at 5 rad/s. Fig. 15(a) shows that $\sigma_{\omega r}$ for the signal-injection-aided drive is 8.8% of that for the standard VTO-based drive at 14 rad/s. In general, whenever signal injection is used, $\sigma_{\omega r}$ is independent from the resolution of the position sensing system and the VTO can be tuned much more aggressively, thereby providing strongly beneficial effects on drive performance in the low-speed range.

Fig. 16 shows the speed command tracking performance when a 1 BPP resolution is used, in conjunction with the signal-injection-aided VTO. The speed command starts at 0 rad/s, then switches to -10 rad/s, $+10$ rad/s and then back to 0 rad/s. The drive is able to track the variations in the speed command, within the motion controller bandwidth. It is worth mentioning that this performance is not possible without signal injection, because a 1 BPP position sensing system alone cannot recognize variations in the direction of rotation, as explained in Section II.

B. Load Tests

Disturbance response tests have been performed to evaluate the disturbance rejection capability of the drive. For these tests, the motor has been connected to a torque-controlled dc drive. The tests are carried out with a fixed speed command set to 10 rad/s and a 0.4 p.u. step load torque applied to the shaft. Higher step load torques have not been applied because drive stability is compromised when high-frequency injection is deactivated. The VTO is tuned to have a 20 Hz bandwidth. Fig. 17 shows ω_r, $\omega_{r\_\mathrm{VTO\_unenh}}$, and i_q following the step load when signal injection is not used. As expected, the disturbance response deteriorates as the resolution drops from 3 BPP to 1 BPP. The drive however always recovers and does not lose stability. This is ascribable to the stabilizing effect of the inertia of the dc machine load. Fig. 18 shows the disturbance response when the signal-injection-aided VTO is used. The response is much smoother, and the drive recovers the commanded speed more quickly. It can be noted that there are no significant differences in the responses associated to 3, 2, or 1 BPP, thanks to the signal injection. Fig. 19 shows a speed ramp from 0 to 60 rad/s in 0.5 s, at 0.6 p.u. load. The drive is equipped with a 3 BPP sensing system. At 30 rad/s, the high-frequency signal injection is removed and the VTO operates with the Hall-effect sensor inputs only. It can be seen that the instantaneous transition to sensor-only operation does not cause any visible effect and the drive continues to operate very smoothly. This is due to the fact that the switch is performed at a speed at which the position sample rate of the sensors is sufficiently high to guarantee correct position tracking and quantization harmonic decoupling in the VTO.

C. Hall-Effect Sensor Fault Tests

Experimental tests have also been performed to evaluate the performance of the position sensing system following sensor faults at low speeds. Consistently with the simulations performed in Section IV-C, a 3 BPP system has been used, together with the same fault detection, identification, and compensation algorithm. Fig. 20(a) shows the performance of the drive following the emulation of two successive faults, at 0.6 p.u. load and at 20 rad/s commanded speed. For this test, no signal

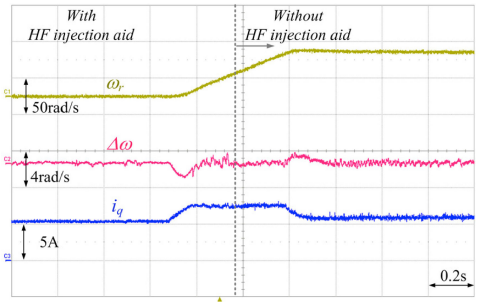

Fig. 19. Speed transient from 0 to 60 rad/s, at 0.6. p.u. load, when the drive is equipped with a 3 BPP position sensing system.

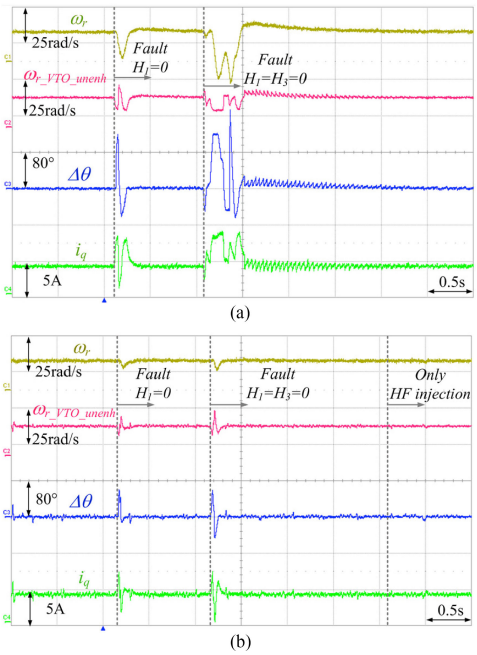

Fig. 20. Performance of the drive equipped with a 3 BPP sensing system, following two successive sensor faults at 20 rad/s. (a) Without signal injection. (b) With signal injection.

injection was used. It can be seen that the position estimation error exceeds 90° electrical in both of the post-fault transients. As predicted by the simulations, the second sensor fault produces considerable rotor oscillations before compensation is obtained. As expected, Fig. 20(b) shows the significantly improved performance following the same faults, when the signal-injection-aided VTO is used. In this case the maximum position estimation error is around 60° electrical and the rotor does not undergo any oscillation.

Following the second sensor fault, only one Hall-effect sensor is working correctly. Depending on the strategy, operation can continue with the single sensor or the sensor can be deactivated, and limp-home mode can be entered by switching to self-sensing alone. As an example, Fig. 20(b) shows a transition to high-frequency injection self-sensing, about 2 s after the compensation of the second fault: no influence on the drive performance can be seen. In the event that the second fault were to occur at higher speeds, a transition to back-EMF-based self-sensing can be easily implemented.

VI. Conclusion

This paper has shown that binary Hall-effect sensor-based position sensing systems are strong candidates for use in PMSM drives operating in safety-critical applications, for which self-sensing alone is not allowed and the use of a highly reliable position sensor is mandatory. The key conclusions can be summarized as follows.

1) Binary Hall-effect-based sensing systems possess much higher MTTFs and much lower failure rates than high resolution position sensors, at a much lower cost.
2) As long as the machine possesses sufficient electromagnetic saliency, high-frequency signal injection can be easily merged with binary Hall-effect-based sensing systems, by forming a signal-injection-aided VTO; this allows to achieve a low-speed performance similar to that obtained with high-resolution sensors.
3) An operating point model of the signal-injection-aided VTO has been derived, which shows that, when signal injection is present, the VTO is forced to track the rotor position as sensed by the high-frequency injection.
4) Transition to operation without signal-injection can be done at speeds above 0.1 p.u., by simply de-activating the signal injection contribution or by implementing a smooth, speed-dependent transition.
5) Simulations and experimental results have demonstrated how the use of the signal-injection-aided VTO removes low-speed instability, allows to maintain constant VTO gains throughout the entire speed range, considerably improves speed command tracking and also allows a much faster recovery of the drive following Hall-effect sensor faults at low speeds.

References

[1] Baumer Group, "Sine encoders ITD22H00 SIL," Baumer Group, Frauenfeld, Switzerland, Datasheet, Jan. 2018. [Online]. Available: https://www.baumer.com/be/en/product-overview/rotary-encoders-angle-sensors/industrial-encoders-incremental/sincos/itd22h00-sil/p/medias/__secure__/Baumer_ITD22H00_SIL_DS_EN.pdf
[2] Kollmorgen, "Safety characteristic data." 2018. [Online]. Available: https://kdn.kollmorgen.com/content/Safety-Characteristic-Data. Accessed on: Jun. 7, 2018.
[3] A. Boglietti, A. Cavagnino, A. Tenconi, and S. Vaschetto, "The safety critical electric machines and drives for the more electric aircraft: A survey," in *Proc. IEEE IECON*, Nov. 2009, pp. 2587–2594.
[4] C. Ebert, "Implementing functional safety," *IEEE Softw.*, vol. 32, no. 5, pp. 84–89, 2015.
[5] *Functional Safety of Electrical/Electronic/Programmable Electronic Safety-Related Systems*, IEC Standard 61508, 2010.
[6] *Road Vehicles–Functional Safety*, ISO Standard 26262, 2011.
[7] D. J. K. Griffin and G. Bearfield, "The use of design targets in harmonisation of safety management in the European rail industry," in *Risk, Reliability and Safety: Innovating Theory and Practice*, L. Walls, M. Revie, and T. Bedford, Eds. Boca Raton, FL, USA: CRC Press, 2016, pp. 1299–1305.
[8] J. Schwarz, *Functional safety and automotive software; Introduction ISO 26262 at Daimler*, Daimler AG, Stuttgart, Germany, Sep. 2012. [Online]. Available: https://www.ipa.go.jp/files/000004100.pdf. Accessed on: Dec. 17, 2017.
[9] J. Birch *et al.*, "Safety cases and their role in ISO 26262 functional safety assessment," in *Computer Safety, Reliability, and Security. SAFECOMP 2013 (Lecture Notes in Computer Science* 8153), F. Bitsch, J. Guiochet, and M. Kaâniche, Eds. Berlin, Heidelberg: Springer, 2013.
[10] C. Ebert, "Functional Safety with ISO 26262," *Vector Consulting Services GmbH*, Stuttgart, Germany, Oct. 2016. [Online]. Available: https://vector.com/portal/medien/vector_consulting/publications/Webinar_Safety.pdf. Accessed on: Dec. 17, 2017.

[11] H. Kwon, R. Itabashi-Campbell, and K. McLaughlin, "ISO26262 application to electric steering development with a focus on hazard analysis," in *Proc. IEEE SysCon*, Apr. 2013, pp. 655–661.

[12] G. El Murr, A. Griffo, J. Wang, Z. Q. Zhu, and B. Mecrow, "Reliability assessment of fault tolerant permanent magnet AC drives," in *Proc. IEEE IECON*, Nov. 2015, pp. 2777–2782.

[13] J. W. Bennet *et al.*, "A prototype electrical actuator for aircraft flaps and slats," in *Proc. IEEE IEMDC*, May 2005, pp. 41–47.

[14] Honeywell, "High sensitivity latching digital Hall-effect sensor ICs: SS360NT, SS360ST, SS360ST-10K, SS460S, SS460S-T2, SS460S-LP," Honeywell International Inc., Morris Plains, New Jersey, USA, Rep. 32312441-B, Datasheet, Jul. 2016.

[15] K. A. Corzine and S. D. Sudhoff, "A hybrid observer for high performance brushless DC motor drives," *IEEE Trans. Energy Conv.*, vol. 11, no. 2, pp. 318–323, Jun. 1996.

[16] S. Morimoto, M. Sanada, and Y. Takeda, "Sinusoidal current drive system of permanent magnet synchronous motor with low resolution position sensors," in *Conf. Rec. IEEE IAS Annu. Meeting*, Oct. 1996, pp. 9–13.

[17] T. D. Batzel and K.-Y. Lee, "Slotless permanent magnet synchronous motor without a high resolution rotor angle sensor," *IEEE Trans. Energy Conv.*, vol. 15, no. 4, pp. 366–371, Dec. 2000.

[18] H. Kim, S. Yi, N. Kim, and R. D. Lorenz, "Using low resolution position sensors in bumpless position/speed estimation methods for low cost PMSM drives," in *Conf. Rec. IEEE IAS Annu. Meeting*, Oct. 2005, pp. 2518–2525.

[19] F. G. Capponi, G. De Donato, L. D. Ferraro, O. Honorati, M. C. Harke, and R. D. Lorenz, "AC brushless drive with low-resolution Hall-effect sensors for surface-mounted PM machines," *IEEE Trans. Ind. Appl.*, vol. 42, no. 2, pp. 526–535, Mar./Apr. 2006.

[20] A. Lidozzi, L. Solero, F. Crescimbini, and A. Di Napoli, "SVM PMSM drive with low resolution Hall-effect sensors," *IEEE Trans. Power Electron.*, vol. 22, no. 1, pp. 282–290, Jan. 2007.

[21] M. C. Harke, G. De Donato, F. G. Capponi, T. R. Tesch, and R. D. Lorenz, "Implementation issues and performance evaluation of sinusoidal, surface-mounted PM machine drives with Hall-effect position sensors and a vector-tracking observer," *IEEE Trans. Ind. Appl.*, vol. 44, no. 1, pp. 161–173, Jan./Feb. 2008.

[22] T. R. Tesch and R. D. Lorenz, "Disturbance torque and motion state estimation with low-resolution position interfaces using heterodyning observers," *IEEE Trans. Ind. Appl.*, vol. 44, no. 1, pp. 124–134, Jan./Feb. 2008.

[23] G. De Donato, M. C. Harke, F. G. Capponi, and R. D. Lorenz, "Sinusoidal surface-mounted pm machine drive using a minimal resolution position encoder," in *Proc. IEEE APEC*, Feb. 2008, pp. 104–110.

[24] A. Yoo, S.-K. Sul, D.-C. Lee, and C.-S. Jun, "Novel speed and rotor position estimation strategy using a dual observer for low-resolution position sensors," *IEEE Trans. Power Electron.*, vol. 24, no. 12, pp. 2897–2906, Dec. 2009.

[25] G. Scelba, G. De Donato, G. Scarcella, F. G. Capponi, and F. Bonaccorso, "Fault-tolerant rotor position and velocity estimation using binary Hall-effect sensors for low-cost vector control drives," *IEEE Trans. Ind. Appl.*, vol. 50, no. 5, pp. 1629–1636, Sep./Oct. 2014.

[26] G. Scelba, G. De Donato, M. Pulvirenti, F. G. Capponi, and G. Scarcella, "Hall-effect sensor fault detection, identification and compensation in brushless DC drives," *IEEE Trans. Ind. Appl.*, vol. 522 no. 2, pp. 1542–1554, Mar./Apr. 2016.

[27] G. De Donato, G. Scelba, M. Pulvirenti, G. Scarcella, and F. G. Capponi, "Signal-injection-aided position and speed estimation for PMSM drives with low-resolution position sensors," in *Proc. IEEE ECCE*, Sep. 2016, pp. 2489–2495.

[28] R. D. Lorenz, T. A. Lipo, and D. W. Novotny, "Motion control with induction motors," *Proc. IEEE*, vol. 82, no. 8, pp. 1215–1240, Aug. 1994.

[29] H. Kim, M. C. Harke, and R. D. Lorenz, "Sensorless control of interior permanent-magnet machine drives with zero-lag position estimation," *IEEE Trans. Ind. Appl.*, vol. 39, no. 6, pp. 1726–1733, Nov./Dec. 2003.

[30] R. W. Hejny and R. D. Lorenz, "Evaluating the practical low-speed limits for back-emf tracking-based sensorless speed control using drive stiffness as a key metric," *IEEE Trans. Ind. Appl.*, vol. 47, no. 3, pp. 1337–1343, May/Jul. 2011.

[31] A. Consoli, G. Scarcella, G. Scelba, A. Testa, and D. A. Triolo, "Sensorless rotor position estimation in synchronous reluctance motors exploiting a flux deviation approach," *IEEE Trans. Ind. Appl.*, vol. 43, no. 5, pp. 1266–1273, Sep./Oct. 2007.

[32] A. Consoli, G. Scarcella, G. Scelba, A. Testa, and S. Royak, "Phase modulation-based technique for saliency position estimation of IPMSMs," in *Proc. IEEE ECCE*, Sep. 2009, pp. 2489–2495.

[33] H. W. De Kock, M. J. Kamper, and R. M. Kennel, "Anisotropy comparison of reluctance and PM synchronous machines for position sensorless control using HF carrier injection," *IEEE Trans. Power Electron.*, vol. 24, no. 8, pp. 1905–1913, Aug. 2009.

[34] D. Raca, P. García, D. D. Reigosa, F. Briz, and R. D. Lorenz, "Carrier-signal selection for sensorless control of PM synchronous machines at zero and very low speeds," *IEEE Trans. Ind. Appl.*, vol. 46, no. 1, pp. 167–178, Jan./Feb. 2010.

[35] F. M. L. De Belie, P. Sergeant, and J. A. Melkebeek, "A sensorless drive by applying test pulses without affecting the average-current samples," *IEEE Trans. Power Electron.*, vol. 25, no. 4, pp. 875–888, Apr. 2010.

[36] F. Briz and M. W. Degner, "Rotor position estimation," *IEEE Ind. Electron. Mag.*, vol. 5, no. 2, pp. 24–36, Jun. 2011.

[37] Y.-D. Yoon, S.-K. Sul, S. Morimoto, and K. Ide, "High-bandwidth sensorless algorithm for AC machines based on square-wave-type voltage injection," *IEEE Trans. Ind. Appl.*, vol. 47, no. 3, pp. 1361–1370, May./Jun. 2011.

[38] G. Scarcella, G. Scelba, and A. Testa, "High performace sensorless controls based on HF excitation: A viable solution for future AC motor drives?" in *Proc. IEEE WEMDCD*, Mar. 2015, pp 178–187.

[39] A. Piippo and J. Luomi, "Adaptive observer combined with HF signal injection for sensorless control of PMSM drives," in *Proc. IEEE IEMDC*, May 2005, pp. 674–681.

[40] S. Wu, D. D. Reigosa, Y. Shibukawa, M. A. Leetmaa, R. D. Lorenz, and Y. Li, "Interior permanent-magnet synchronous motor design for improving self-sensing performance at very low speed," *IEEE Trans. Ind. Appl.*, vol. 45, no. 6, pp. 1939–1946, Nov./Dec. 2009.

[41] Z. Q. Zhu and L. M. Gong, "Investigation of effectiveness of sensorless operation in carrier-signal-injection-based sensorless-control methods," *IEEE Trans. Ind. Electron.*, vol. 58, no. 8, pp. 3431–3439, Aug. 2011.

[42] P. L. Jansen and R. D. Lorenz, "Transducerless position and velocity estimation in induction and salient AC machines," *IEEE Trans. Ind. Appl.*, vol. 32, no. 6, pp. 1380–1393, Nov./Dec. 1996.

[43] S. Bolognani, S. Calligaro, R. Petrella, and M. Tursini, "Sensorless control of IPM motors in the low-speed range and at standstill by HF injection and DFT processing," *IEEE Trans. Ind. Appl.*, vol. 47, no. 1, pp. 96–104, Jan./Feb. 2011.

[44] F. Briz, M. W. Degner, P. García, and R. D. Lorenz, "Comparison of saliency-based sensorless control techniques for AC machines," *IEEE Trans. Ind. Appl.*, vol. 40, no. 4, pp. 1107–1115, Jul./Aug. 2004.

[45] P. Sergeant, F. De Belie, and J. Melkebeek, "Rotor geometry design of interior PMSMs with and without flux barriers for more accurate sensorless control," *IEEE Trans. Ind. Electron.*, vol. 59, no. 6, pp. 2457–2465, Jun. 2012.

[46] O. Wallmark and L. Harnefors, "Sensorless control of salient PMSM drives in the transition region," *IEEE Trans. Ind. Electron.*, vol. 53, no. 4, pp. 1179–1187, Aug. 2006.

[47] J.-H. Jang, J.-I. Ha, M. Ohto, K. Ide, and S.-K. Sul, "Analysis of permanent-magnet machine for sensorless control based on high-frequency signal injection," *IEEE Trans. Ind. Appl.*, vol. 40, no. 6, pp. 1595–1604, Nov./Dec. 2004.

[48] A. Eilenberger, E. Schmidt, and M. Schrödl, "Sensorless capability of permanent magnet synchronous machines due to saturation- and reluctance-based coupling effects," in *Proc. IEEE SLED*, Jul. 2010, pp. 14–17.

[49] Z. Ma, J. Gao, and R. Kennel, "FPGA implementation of a hybrid sensorless control of SMPMSM in the whole speed range," *IEEE Trans. Ind. Informat.*, vol. 9, no. 3, pp. 1253–1261, Aug. 2013.

[50] T. C. Lin and Z. Q. Zhu, "Sensorless operation capability of surface-mounted permanent-magnet machine based on high-frequency signal injection methods," *IEEE Trans. Ind. Appl.*, vol. 51, no. 3, pp. 2161–2171, May/Jun. 2015.

[51] J.-H. Jang, S.-K. Sul, J.-I. Ha, K. Ide, and M. Sawamura, "Sensorless drive of surface-mounted permanent-magnet motor by high-frequency signal injection based on magnetic saliency," *IEEE Trans. Ind. Appl.*, vol. 39, no. 4, pp. 1031–1039, Jul./Aug. 2003.

[52] K. Lu, M. Vetuschi, P. O. Rasmussen, and A. E. Ritchie, "Determination of high-frequency d- and q- axis inductances for surface-mounted permanent-magnet synchronous machines," *IEEE Trans. Instrum. Meas.*, vol. 59, no. 9, pp. 2376–2382, Sep. 2010.

[53] E. H. S. Diao, "Fault tolerant control for critical machine-inverter systems used in the automotive industry," Ph.D. dissertation, Univ. Paris-Sud, Paris, France, 2014.

[54] L. Chen, G. Götting, and I. Hahn, "DC-link current and torque ripple optimized self-sensing control of interior-permanent magnet synchronous machines," in *Proc. ICEM*, Sep. 2016, pp. 1029–1035.
[55] E. Dehghan-Azad, S. Gadoue, D. Atkinson, H. Slater, P. Barrass, and F. Blaabjerg, "Sensorless control of IM based on stator-voltage MRAS for limp-home EV applications," *IEEE Trans. Power Electron.*, vol. 33, no. 3, pp. 1911–1921, Mar. 2018.
[56] P. D. T. O'Connor and A. Kleyner, *Practical Reliability Engineering*, 5th ed. Chichester, U.K.: Wiley, 2012.
[57] E. Chiodo and D. Lauria, "Some basic properties of the failure rate of redundant reliability systems on industrial electronics applications," *IEEE Trans. Ind. Electron.*, vol. 62, no. 8, pp. 5055–5062, Aug. 2015.
[58] L. C. Cadwallader, "Reliability estimates for selected sensors in fusion applications," INL, Idaho Falls, ID, Rep. INEL96/0295, Sep. 1996.
[59] Maxim Integrated Products, "Reliability report for Max9621AUB+T," Maxim Integrated Products. 2012. [Online]. Available: https://www.maximintegrated.com/en/reliability/product/MAX9621.pdf. Accessed on: Jun. 7, 2018.
[60] Application Center Staff, "Product reliability report for SS495A," *Honeywell Sensing Control Division*, Freeport, Illinois, 2000.

Giulio De Donato (S'05–M'08–SM'17) was born in Cork, Ireland, in 1978. He received the M.S. and Ph.D. degrees in electrical engineering from the University of Rome "La Sapienza," Rome, Italy, in 2003 and 2007, respectively.

From 2007 to 2008, he was a Research Associate with the Department of Electrical Engineering, University of Rome "La Sapienza," where, from 2008 to 2010, he was an Assistant Professor, and since 2010, he has held the same position with the Department of Astronautical, Electrical, and Energy Engineering (DIAEE). He is co-PI of a collaborative research agreement between the DIAEE and the Department of Electrical, Electronic Engineering, and Computer Science, University of Catania, for research in the field of wide-bandgap-semiconductor-based drives. His current research interests include digital control of brushless drives, analysis and design of permanent-magnet machines, and wide-bandgap-semiconductor-based power converters.

Prof. De Donato is a Member of the IEEE Industry Applications, the IEEE Industrial Electronics, and the IEEE Power Electronics Societies. He is a Member of the IEEE IAS Industrial Drives Committee, the IAS Electric Machines Committee, the IES Electrical Machines Committee, and the PELS Technical Committee on Motor Drives and Actuators. He was the recipient of the 2014 First Prize Paper Award and the 2016 Third Prize Paper Award, both from the IAS Industrial Drives Committee. He is currently an Associate Editor for the IEEE TRANSACTIONS ON INDUSTRY APPLICATIONS.

Giacomo Scelba (S'04–M'07–SM'17) was born in Caltagirone, Italy, in 1976. He received the M.S. and Ph.D. degrees in electrical engineering from the University of Catania, Catania, Italy, in 2002 and 2006, respectively.

He is currently an Assistant Professor in the Department of Electrical, Electronic Engineering, and Computer Science (DIEEI), University of Catania. His research activity was initially focused on sensorless control, digital signal processing, and ac drive control technologies. His current research interests include fault-tolerant motor drives, control techniques for renewable energy systems, and advanced power electronics converters for motor drive applications. He is co-PI of a collaborative research agreement between the DIEEI and the Department of Astronautical, Electrical, and Energy Engineering, University of Rome "La Sapienza," for research in the field of wide-bandgap-semiconductor-based drives.

Prof. Scelba is a Member of the IEEE Industry Applications, the IEEE Industrial Electronics, and the IEEE Power Electronics Societies. He is a Member of the IEEE IAS Industrial Drives Committee. He was the recipient of the 2014 First Prize Paper Award and the 2016 Third Prize Paper Award, both from the IAS Industrial Drives Committee. He is currently an Associate Editor for the IEEE TRANSACTIONS ON INDUSTRY APPLICATIONS.

Mario Pulvirenti (S'13–M'17) was born in Catania, Italy, in 1987. He received the B.S., the M.S., and the Ph.D. degrees in electrical engineering from the University of Catania, Catania, in 2010, 2012 and 2016, respectively.

He spent six months as a Visiting Research Scholar at the University of Wisconsin, Madison, WI, USA, in 2014. In 2016, he was a Research Associate with the Department of Electrical, Electronic Engineering, and Computer Science, University of Catania, where he was engaged in researching the optimal control and fault-tolerant capability of multiphase and multidrive ac systems. Since 2017, he has been with STMicroelectronics, Catania, working with the "Power Transistor Division," on the development and characterization of SiC MOSFET-based applications.

Giuseppe Scarcella (S'98–M'99–SM'17) received the M.S. and Ph.D. degrees both in electrical engineering from the University of Catania, Catania, Italy, in 1995 and 1999, respectively.

In 1995, he was the recipient of an SGS Thomson (now ST Microelectronics) Research Grant. In 1998, he spent a period at the University of Wisconsin, Madison, WI, USA, working on sensorless control of electrical drives. In 1999, he joined the Department of Electrical, Electronic, and Systems Engineering, University of Catania, as a Temporary Researcher. In 2001, he obtained a permanent position as an Assistant Professor, in the same department, where, since 2005, he is an Associate Professor in the areas of power electronics, electrical machines, and drives. He is the author of over 180 technical papers published on journals and proceedings of national and international conferences and holds several international patents. His current research interests include sensorless control of electrical machines, advanced control, digital modulation techniques, efficiency optimization techniques, and electromagnetic compatibility.

Prof. Scarcella is a Member of the IEEE Industry Applications Society. He was the recipient of the 1998 Third Prize Paper Award, the 2014 First Prize Paper Award, and the 2016 Third Prize Paper Award from the IAS Industrial Drives Committee and the IEEE Transactions on Power Electronics Best Paper Award in 2000.

Fabio Giulii Capponi (M'98) received the M.S. and Ph.D. degrees in electrical engineering from the University of Rome "La Sapienza," Rome, Italy, in 1994 and 1998, respectively.

From 1996 to 2015, he was an Assistant Professor with the University of Rome "La Sapienza," where he is currently an Associate Professor of Electrical Machines, Converters, and Drives in the Department of Astronautical, Electrical, and Energy Engineering. In 2003 and 2004, he was a Visiting Scholar at the Wisconsin Electrical Machines and Power Electronics Consortium (WEMPEC), University of Wisconsin, Madison, WI, USA. He is author or co-author of more than 90 published technical papers. His current research interests include permanent magnet motor drives and multi-physics design of electrical machines.

Prof. Giulii Capponi is a Registered Professional Engineer in Italy and is Member of the IEEE Industry Applications, the IEEE Industrial Electronics, and the IEEE Power Electronics Societies. He is a Member of the IEEE IAS Industrial Drives Committee, the Electric Machines Committee, and the Transportation Systems Committee. He received the 2014 First Prize Paper Award and the 2016 Third Prize Paper Award, both from the IAS Industrial Drives Committee.